Supplementary Document for

“High Flux Passive Imaging with Single-Photon Sensors”

Atul Ingle, Andreas Velten†, Mohit Gupta†

Correspondence to: ingle@uwalumni.com

CVPR 2019

Supplementary Note 1. Image Formation Model and Flux Estimator for a PF-SPAD Pixel

A PF-SPAD sensor pixel and a time-correlated photon counting module are used to obtain total photon counts over a fixed exposure time together with picosecond resolution measurements of the time elapsed between successive photon detection events. We will assume that the PF-SPAD pixel is exposed to a true photon flux of Φ photons/second for an exposure time of T seconds and it records N_T photons in exposure time interval $(0, T]$. For mathematical convenience, we assume that the exposure interval starts with a photon detection event at time $t = 0$.

Photons arrive at the SPAD according to a Poisson process. Accounting for an imperfect photon detection efficiency of $0 < q < 1$, the time between consecutive incident photons follows an exponential distribution with rate $q\Phi$. After each detection event, the SPAD enters a dead time window of duration τ_d. Due to the memoryless property of Poisson processes [6], the time interval between the end of a dead time window and the next photon arrival is also exponentially distributed and has the same rate $q\Phi$ as the incident Poisson process. Let X_1 be the time of the first photon detection after $t = 0$ and X_n be the time between the $n-1^{st}$ and n^{th} detection event for $n \geq 2$. Then the inter-detection time duration X_n follows a *shifted* exponential distribution given by:

$$X_n \overset{iid}{\sim} f_{X_n}(t) = \begin{cases} q\Phi e^{-q\Phi(t-\tau_d)} & \text{for } t \geq \tau_d \\ 0 & \text{otherwise.} \end{cases} \tag{S1}$$

This provides a probabilistic model of the photon inter-detection times. We now derive a flux estimator from a sequence of observed inter-detection times captured by a PF-SPAD pixel.

Estimating Flux from Inter-Detection Time Intervals

The log-likelihood function for the observed inter-detection times is given by

$$\begin{aligned} \log l(q\Phi; X_1, \ldots, X_{N_T}) &= \log\left(\prod_{n=1}^{N_T} q\Phi\, e^{-q\Phi(X_n-\tau_d)}\right) \\ &= -q\Phi\left(\sum_{n=1}^{N_T} X_n - \tau_d N_T\right) + N_T \log q\Phi \\ &= -q\Phi\, N_T\, \left(\bar{X} - \tau_d\right) + N_T \log q\Phi \end{aligned} \tag{S2}$$

where $\bar{X} := \frac{1}{N_T}\sum_{n=1}^{N_T} X_n$ is the mean time between photon detection events. The maximum likelihood estimate $\hat{\Phi}$ of the true photon flux is computed by setting the derivative of Equation (S2) to zero:

$$\frac{N_T}{q\hat{\Phi}} - N_T(\bar{X} - \tau_d) = 0$$

which implies

$$\hat{\Phi} = \frac{1}{q}\frac{1}{\bar{X} - \tau_d}. \tag{S3}$$

†Equal contribution.

Supplementary Note 2. Approximate Closed Form Formula for SNR of a PF-SPAD pixel

We first derive an approximate formula for the SNR of a PF-SPAD pixel using a continuous Gaussian distribution approximation for the number of counts N_T. The effective incident photon flux for a quantum efficiency of $0 < q < 1$ is equal to $q\Phi$ photons/second.

The random process describing the detections of this PF-SPAD pixel is not a Poisson process, but can be modeled as a renewal process [6] with a shifted exponential inter-arrival distribution which has a mean $\tau_d + \frac{1}{q\Phi}$ and variance $\frac{1}{q^2\Phi^2}$. Using the central limit theorem for renewal processes, N_T is approximately Gaussian distributed with mean:

$$\mathbf{E}[N_T] = \frac{q\Phi T}{1 + q\Phi\tau_d}$$

and variance:

$$\mathrm{Var}[N_T] = \frac{q\Phi T}{(1 + q\Phi\tau_d)^3}.$$

Quantization Noise: An additional source of variance arises due to quantization noise which we can treat as uniformly distributed between 0 and 1 with variance $1/12$. The c.d.f. of the estimated photon flux $\hat{\Phi}$ can be computed using the delta method [3]:

$$\begin{aligned}
F_{\hat{\Phi}}(x) &= \mathsf{Pr}(\hat{\Phi} \le x) && \text{(S4)}\\
&= \mathsf{Pr}\left(\frac{1}{q}\frac{N_T}{T - \tau_d N_T} \le x\right) && \text{(S5)}\\
&\approx \mathsf{Pr}\left(N_T \le \frac{qxT}{1 + qx\tau_d}\right) && \text{(S6)}\\
&= \frac{1}{2}\left(1 + \mathrm{erf}\left(\frac{\frac{qxT}{1+qx\tau_d} - \frac{q\Phi T}{1+q\Phi\tau_d}}{\sqrt{2}\sqrt{\frac{q\Phi T}{(1+q\Phi\tau_d)^3} + \frac{1}{12}}}\right)\right) && \text{(S7)}\\
&\approx \frac{1}{2}\left(1 + \mathrm{erf}\left(\frac{x - \Phi}{\sqrt{2}\sqrt{\frac{\Phi(1+q\Phi\tau_d)}{qT} + \frac{(1+q\Phi\tau_d)^4}{12q^2T^2}}}\right)\right) && \text{(S8)}
\end{aligned}$$

where Equation (S6) follows from the fact that in practice the denominator is always non-negative since $N_T \le \lfloor T/\tau_d \rfloor$, Equation (S7) follows from the formula for the Gaussian c.d.f. of N_T with erf denoting the error function [1], and Equation (S8) is follows from a first order Taylor series approximation. This result shows that $\hat{\Phi}$ is approximately normally distributed with mean equal to the true photon flux and variance given by the denominator in Equation (S8).

Dark Count and Afterpulsing Bias: In addition to quantization and shot noise that introduce variance in the estimated photon flux, PF-SPADs also suffer from dark counts and afterpulsing noise that introduce a bias in the estimated flux. The dark count rate Φ_{dark} is often given in published datasheets and can be used as the bias term. Afterpulsing noise is quoted in datasheets as afterpulsing probability which denotes the probability of observing a spurious afterpulse after the dead time τ_d has elapsed. Due to an exponentially distributed waiting time, the probability of observing a gap between true photon-induced avalanches is equal to $e^{-q\Phi\tau_d}$. A fraction $p_{\text{ap}}e^{-q\Phi\tau_d}$ of these gaps will contain afterpluses, on average. The bias $\Delta\hat{\Phi}$ in the estimated flux is given by:

$$\Delta\hat{\Phi} = \hat{\Phi}\frac{T}{T - N_T\tau_d}\frac{\Delta N_T}{N_T} = \frac{T}{T - N_T\tau_d}p_{\text{ap}}e^{-q\Phi\tau_d} = q\Phi(1 + \Phi\tau_d)p_{\text{ap}}e^{-q\Phi\tau_d}. \tag{S9}$$

Using the bias-variance decomposition of mean-squared error, we have

$$\mathsf{RMSE}(\hat{\Phi}) = \sqrt{(\Phi_{\text{dark}} + q\Phi(1 + \Phi\tau_d)p_{\text{ap}}e^{-q\Phi\tau_d})^2 + \frac{\Phi(1 + q\Phi\tau_d)}{qT} + \frac{(1 + q\Phi\tau_d)^4}{12q^2T^2}} \tag{S10}$$

and the approximate closed from SNR is obtained by plugging Equation (S10) into Equation (9) in the main text.

Supplementary Note 3. Exact Formula for Numerical Computation of SNR of a SPAD Pixel

It is possible to model the exact discrete distribution of the number of counts N_T for a PF-SPAD pixel using non-asymptotic renewal theory. The times between consecutive counts for a PF-SPAD pixel can be modeled as a shifted exponential distribution as before. Let X_n be the time between when the SPAD detects the $(n-1)^{st}$ and n^{th} photons $(n \geq 1)$. For mathematical convenience, we assume $X_0 = 0$. Let F_{S_n} be the c.d.f. of the sum $S_n := \sum_{i=1}^{n} X_n$. Then, by definition, $F_{S_n}(T) = \mathsf{Pr}(N_T \geq n)$. Therefore we can write

$$p_n := \mathsf{Pr}(N_T = n) = F_{S_n}(T) - F_{S_{n+1}}(T)$$

where

$$F_{S_n}(T) = 1 - \sum_{k=0}^{n-1} \frac{(T - n\tau_d)^k (q\Phi)^k}{k!} e^{-(T-n\tau_d)q\Phi} = 1 - Q(n-1, (T - n\tau_d)q\Phi)$$

and $Q(\cdot, \mu)$ is the c.d.f. of a Poisson random variable with rate μ, also known as the regularized gamma function [1]. For convenience, define:

$$Q_{q,\Phi,T,\tau_d}(k) := Q(k, (T - k\tau_d)q\Phi).$$

The following formula can now be used to numerically compute the probability mass function of N_T:

$$p_n = \begin{cases} Q_{q,\Phi,T,\tau_d}(n) - Q_{q,\Phi,T,\tau_d}(n-1) & \text{for } 1 \leq n \leq \lfloor \frac{T}{\tau_d} \rfloor \\ 0 & \text{otherwise.} \end{cases} \tag{S11}$$

Using the bias-variance decomposition, the RMSE can be written as:

$$\mathsf{RMSE}(\hat{\Phi}) = \sqrt{(\Phi_{\text{dark}} + q\Phi(1 + \Phi\tau_d)p_{\text{ap}}e^{-q\Phi\tau_d})^2 + \sum_{n=1}^{\lfloor \frac{T}{\tau_d} \rfloor} p_n \left(\frac{1}{q} \frac{n}{T - n\tau_d} - \Phi \right)^2} \tag{S12}$$

and SNR can be computed by plugging Equation (S11) and Equation (S12) in Equation (9) in the main text. Note that although this formula is exact, it does not lend itself to an intuitive interpretation as the approximate formula in Equation (S10) which decomposes the sources of variance into shot noise and quantization noise.

Supplementary Note 4. Various Sources of Noise Affecting the PF-SPAD Flux Estimate

Various unique properties of the shot noise and quantization noise were discussed in the main text. Another surprising result is that the effect of afterpulsing bias first increases and then decreases with incident photon flux. Recall that afterpulses are correlated with past avalanche events. At very low incident photon flux there are very few photon-induced avalanches which implies that there are even fewer afterpulsing avalanches. At very high photon flux values, the afterpulsing noise is overwhelmed by the large number of true photon-induced avalanches that leave negligible temporal gaps between consecutive dead time windows. However, for most modern SPAD pixels, afterpulsing noise is so small that it can often be ignored. The plot in Supplementary Figure 1 shows an afterpulsing error curve using an unrealistically high afterpulsing rate to accentuate the trend as a function of incident flux.

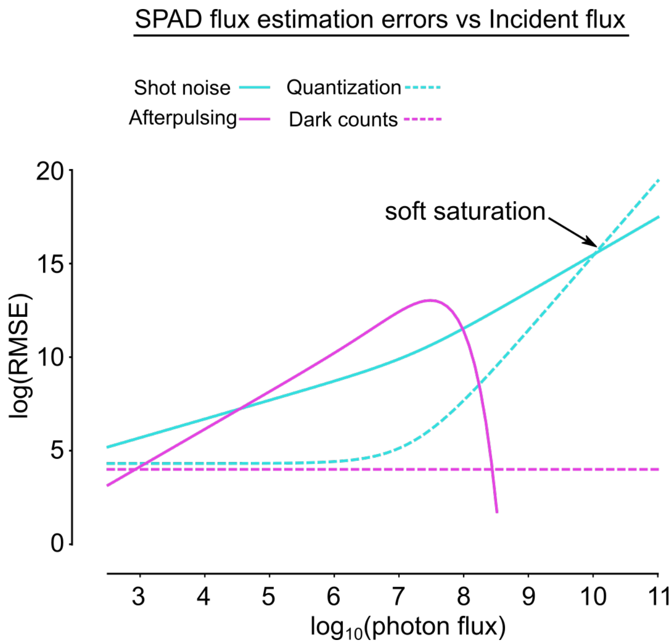

Supplementary Figure 1. **Effect of various sources of noise on the estimated photon flux for a conventional and a SPAD pixel.** This figure shows the contributions to the flux estimation error from various sources of noise in a SPAD pixel. Quantization noise and shot noise were discussed in the main text and in Figure 3. Bias due to afterpulsing noise increases with incident flux and then decreases. Dark count noise remains small and constant at all flux levels. In order to accentuate the trend of afterpulsing error with incident flux, this plot uses an unrealistically high afterpulsing probability of 30%, which is much higher than the 1% probability for our hardware prototype.

Supplementary Note 5. SNR of a Conventional Sensor Pixel

A conventional CCD or CMOS pixel suffers from a hard saturation limit due to its full well capacity, N_{FWC}. Assuming a quantum efficiency of $0 < q < 1$, an incident photon flux of Φ photons/second and an exposure time T seconds, the photon counts N_T follow a Gaussian distribution with mean $q\Phi T$ and variance $q\Phi T + \sigma_r^2$ where σ_r is the read noise of the pixel. The estimated flux is given by [7]:

$$\hat{\Phi}_{\text{CCD}} = \begin{cases} \frac{N_T}{qT}, & N_T < N_{\mathrm{FWC}} \\ \infty, & N_T = N_{\mathrm{FWC}}. \end{cases}$$

The RMSE of the estimated flux is given by:

$$\mathsf{RMSE}(\hat{\Phi}_{\text{CCD}}) = \sqrt{\mathbf{E}[(\hat{\Phi}_{\text{CCD}} - \Phi)^2]} = \begin{cases} \frac{\sqrt{q\Phi T + \sigma_r^2}}{qT}, & \Phi < \frac{N_{\mathrm{FWC}}}{qT} \\ \infty, & \Phi \geq \frac{N_{\mathrm{FWC}}}{qT}. \end{cases}$$

which leads to the following formula for SNR of conventional pixel:

$$\mathsf{SNR}_{\text{CCD}}(\Phi) = \begin{cases} 10\log_{10}\left(\frac{q^2\Phi^2T^2}{q\Phi T + \sigma_r^2}\right), & \Phi < \frac{N_{\mathrm{FWC}}}{qT} \\ -\infty, & \Phi \geq \frac{N_{\mathrm{FWC}}}{qT}. \end{cases} \tag{S13}$$

This formula does not account for dark current noise because it is only relevent at extremely low incident photon flux values with very long exposure times of many minutes or longer.

Supplementary Note 6. Effect of Varying Exposure Time

The notions of quantum efficiency and exposure time are interchangeable in case of conventional image sensors; Equation (S13) remains unchanged if the symbols q and T were to be swapped. This is not true for a PF-SPAD sensor where changing q and changing T has different effects on the overall SNR. This is because the SPAD pixel has an asymptotic saturation limit of T/τ_d counts which is a function of exposure time, unlike a conventional sensor whose full well capacity is a fixed constant independent of exposure time. As shown in Supplementary Figure 2, decreasing exposure time decreases the maximum achievable SNR value of a SPAD sensor. Experimental results were obtained from our hardware prototype using a dead time of $300\,\mathrm{ns}$ and capturing photon counts with two different exposure times of $0.5\,\mathrm{ms}$ and $5\,\mathrm{ms}$.

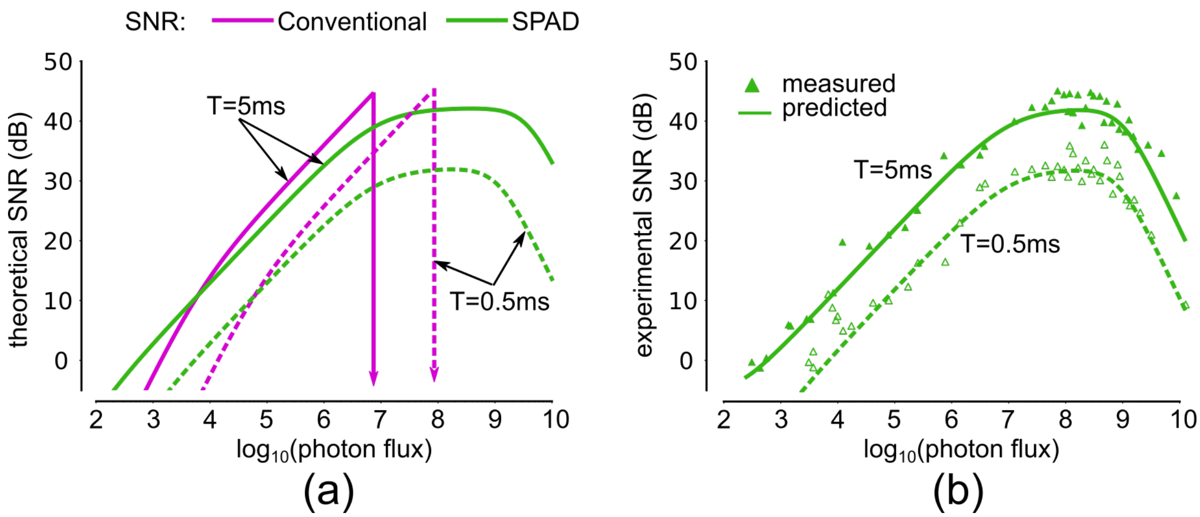

Supplementary Figure 2. **Effect of varying exposure time on SNR** (a) For a conventional sensor, decreasing exposure time translates the SNR curve towards higher photon flux values while keeping the overall shape of the curve same. However, for a PF-SPAD pixel, decreasing exposure time decreases the maximum achievable SNR. (b) Experimental SNR data obtained with two exposure times. The SNR curves decay more rapidly than (a) due to additional dead time uncertainty effects in our hardware prototype, but the decrease in maximum achievable SNR is still clearly seen.

Supplementary Note 7. Details of SPAD Simulation Model and Experimental Setup

We implemented a time-domain simulation model for a PF-SPAD pixel to validate our theoretical formulas for the PF-SPAD response curve and SNR. Photons impinge the simulated PF-SPAD pixel according to a Poisson process; a fraction of these photons are missed due to limited quantum efficiency. The PF-SPAD pixel counts an incident photon when it arrives outside a dead time window. The simulation model also accounts for spurious detection events to dark counts and afterpulsing. The pseudo-code is shown in Supplementary Figure 3.

PF-SPAD and Conventional Sensor Specifications Each pixel in the simulated PF-SPAD array mimics the specifications of the single-pixel hardware prototype. Each pixel in our simulated conventional sensor array uses slightly higher specifications than the one we used in our experiments. It has a full well capacity of 33,400 electrons, quantum efficiency of 90% and read noise of 5 electrons.

The single-pixel SPAD simulator was used for generating synthetic color images from a hypothetical megapixel SPAD array camera. The ground truth photon flux values were obtained from an exposure bracketed HDR image that covered over 10 orders of magnitude in dynamic range. Unlike regular digital images that use 8 bit integers for each pixel value, an HDR image is represented using floating point values that represent the true scene radiance at each pixel. These floating point values were appropriately scaled and used as the ground-truth photon flux to generate a sequence of photon arrival times following Poisson process statistics. Red, green and blue color channels were simulated independently. Results of simulated HDR images are shown in Supplementary Figures 7, 8 and 9.

Input: Φ: true incident photon flux
T: exposure time
q: SPAD pixel photon detection probability (quantum efficiency)
Φ_{dark}: SPAD dark count rate
τ_d: dead time
p_{ap}: afterpulsing probability
Output: N_T: number of photon detections

procedure PFSPADSIMULATOR($\Phi, T, q, \tau_d, p_{\text{ap}}$)
    Reset number of photon detections $N_T \leftarrow 0$
    Reset last detection time $t_{\text{last}} \leftarrow -\infty$
    Reset simulation time $t \leftarrow 0$
    Initialize afterpulse time-stamp array $\mathbf{t}_{\text{ap}} = [\,]$
    while $t \leq T$ **do**
        Process timestamps in the after-pulsing time vector $\mathbf{t}_{\text{ap}}$
        Generate next photon time-stamp $t \leftarrow t + \text{Exp}(q\Phi + \Phi_{\text{dark}})$
        if $t \geq t_{\text{last}} + \tau_d$ **then**
            Append next afterpulse time-stamp to $\mathbf{t}_{\text{ap}}$
            $N_T \leftarrow N_T + 1$
            $t_{\text{last}} \leftarrow t$
        end if
    end while
end procedure

Supplementary Figure 3. **Computational model of a PF-SPAD pixel.**

Experimental Setup Details

The single-pixel SPAD from our hardware prototype has a pitch of $25\,\mu\text{m}$, quantum efficiency of 40%, dark count rate of 100 photons/second and 1% afterpulsing probability. The dead time is programmable and was set to $149.7\,\text{ns}$ and exposure time to $5\,\text{ms}$. This corresponds to an asymptotic saturation limit of 33,400 photons.

Each pixel in our machine vision camera (Point Grey GS3-U3-23S6M-C) has a full well capacity of 32,513 electrons, a peak quantum efficiency of 80% and a Gaussian-distributed read noise with a standard deviation of 6.83 electrons. Note that

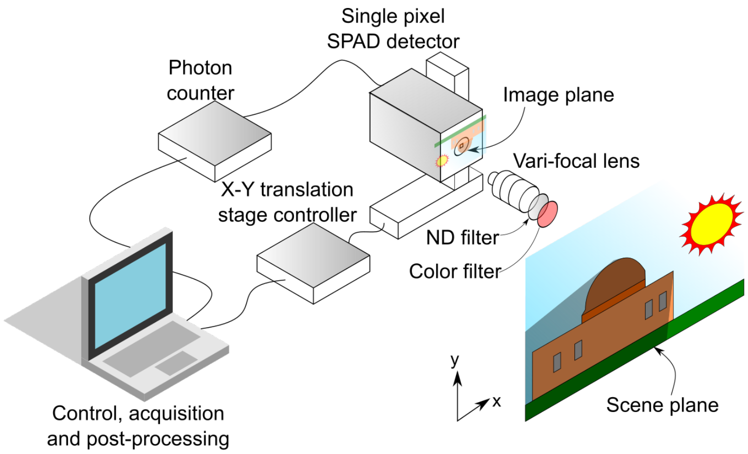

(a)

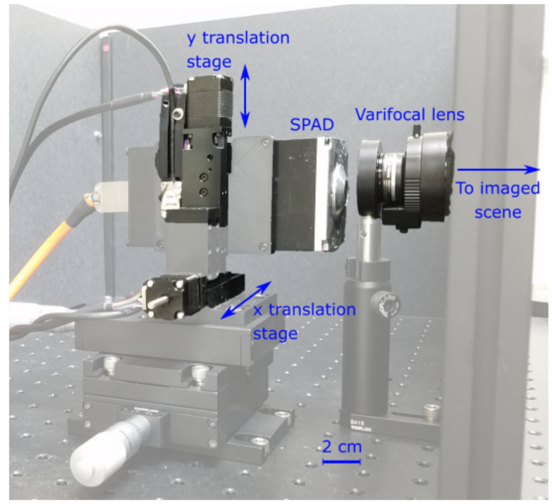

(b)

Supplementary Figure 4. **Experimental setup for raster scanning with a single-pixel PF-SPAD sensor.** (a) The setup consists of a SPAD module mounted on two translation stages, and a variable focal length lens that relays the imaged scene onto the image plane. Photon counts are captured using a free-running time-correlated single-photon counting module operated without a synchronization signal. (b) A picture of our SPAD sensor mounted on the translatation stages.

the asymptotic saturation limit of the PF-SPAD pixel is similar to the full well capacity of this machine vision camera to enable fair comparison.

Supplementary Note 8. Effect of Dead Time Jitter

In practice the dead time window is controlled using digital timer circuits that have a limited precision dictated by the clock speed. The hardware used in our experiments has a clock speed of 167 MHz which introduces a variance of $6\,\mathrm{ns}$ in the duration of the dead time window. As a result the dead time τ_d can no longer be treated as a constant but must be treated as a random variable T_d with mean μ_d and variance σ_d. The inter-arrival distribution in Equation (S1) must be understood as a conditional distribution, conditioned on $T_d = \tau_d$. The mean and variance of the time between photon detections can be computed using the law of iterated expectation [6]:

$$\mathbf{E}[X_n] = \mathbf{E}[\mathbf{E}[X_n|T_d]] = \mu_d + \frac{1}{q\Phi}$$

and

$$\mathrm{Var}[X_n] = \mathbf{E}[(X_n - \mathbf{E}[X_n])^2] = \mathbf{E}[\mathbf{E}[(X_n - \mathbf{E}[\mathbf{E}[X_n|\mathrm{T}_d]])^2|\mathrm{T}_d]] = 1/q^2\Phi^2 + \sigma_d^2.$$

Using similar computations as those leading to Equation (S8), we can derive a modified shot noise variance term equal to $\frac{\Phi(1+q^2\Phi^2\sigma_d^2)(1+q\Phi\mu_d)}{qT}$ that must be used in Equation (S10) to account for dead time variance. All instances of τ_d in Equation (S10) must be replaced by its mean value μ_d. Supplementary Figure 5 shows theoretical SNR curves for a PF-SPAD pixel with a nominal dead time duration of $149.7\,\mathrm{ns}$. Observe that the 30 dB dynamic range degrades by almost 3 orders of magnitude when the dead time jitter increases from $0.01\,\mathrm{ns}$ to $50\,\mathrm{ns}$. For reference, our hardware prototype has a dead time jitter of $6\,\mathrm{ns}$ RMS.

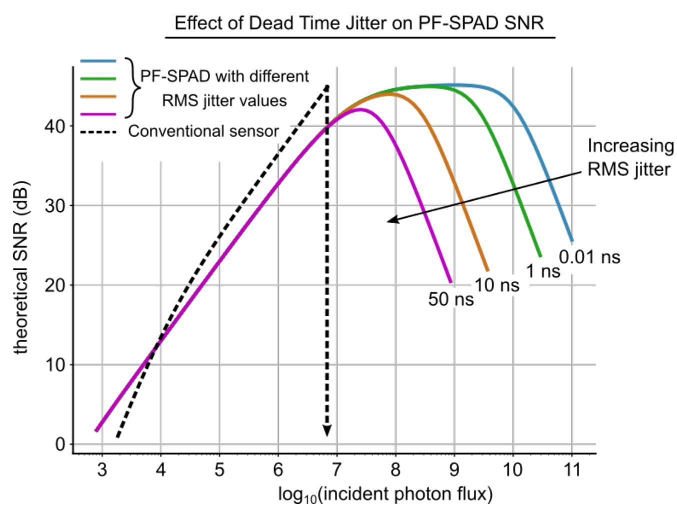

Supplementary Figure 5. **Effect of dead time jitter on PF-SPAD SNR** This figure shows theoretical effect of different values of dead time jitter on the PF-SPAD's SNR is shown. (5 ms exposure time, 149.7 ns dead time, 40% quantum efficiency and 100 Hz dark count rate.)

Supplementary Note 9. Comparison with Quanta Image Sensors

A quanta image sensor (QIS) [4,5,8] improves dynamic range by spatially oversampling the 2D scene intensities using sub-diffraction limit sized pixels called *jots*. Each jot has a limited full well capacity, usually just one photo-electron. The PF-SPAD imaging modality presented in this paper is different from these methods. Instead of using a SPAD as a binary pixel [4] and relying on spatial oversampling, the PF-SPAD achieves dynamic range compression by allowing the dead time windows to shift randomly based on the most recent photon detection time and performing adaptive photon rejection. This is equivalent to the "event-driven recharge" method described in [2].

We now derive the image formation model and an expression for SNR for a QIS and other related methods that use equi-spaced time bins [8], and show that their dynamic range is lower than what can be achieved using a PF-SPAD.

QIS Image Formation and Flux Estimator

The output response of a QIS is logarithmic and mimics silver halide photographic film [5]. Each jot has a binary output, and the final image is formed by spatio-temporally combining groups of jots called a "jot-cube". Let τ_b be the temporal bin width and for mathematical convenience, assume that the exposure time T is an integer multiple of τ_b, so that there are $N = T/\tau_b$ uniformly spaced time bins that split the total exposure duration. Suppose the jot-cube is exposed to a constant photon flux of Φ photons/second, and each jot has a quantum efficiency $0 < q < 1$. The number of photons received by each jot in a time interval τ_b follows a Poisson distribution with mean $q\Phi\tau_b$. Therefore the probability that the binary output of a jot is 0 is given by:

$$\mathsf{Pr}(\text{jot} = 0) = e^{-q\Phi\tau_b}$$

and the probability that the binary output of a jot is 1 is given by the probability of observing 1 or more photons:

$$\mathsf{Pr}(\text{jot} = 1) = 1 - e^{-q\Phi\tau_b}.$$

Let N_T denote the total photon counts output from a jot-cube with N jots. Then N_T follows a binomial distribution given by:

$$\mathsf{Pr}(N_T = k) = \binom{N}{k}(1 - e^{-q\Phi\tau_b})^k (e^{-q\Phi\tau_b})^{N-k},$$

for $0 \leq k \leq N$. The maximum-likelihood estimate of the photon flux is given by:

$$\hat{\Phi}_{\text{QIS}} = \frac{1}{q\tau_b} \log\left(\frac{T}{T - N_T\tau_b}\right). \tag{S14}$$

Our PF-SPAD flux extimator has a higher dynamic range than this uniform binning method. This can be intuitively understood by noting that in the limiting case of $\tau_b = \tau_d$ both schemes have an upper limit on photon counts given by $N_T \leq T/\tau_d$, but the QIS estimator in Equation (S14) saturates and flattens out more rapidly than the PF-SPAD estimator in Equation (2) from the main text:

$$\frac{d\hat{\Phi}_{\text{QIS}}}{dN_T} = \frac{1}{q}\frac{1}{T - N_T\tau_b} < \frac{1}{q}\frac{T}{(T - N_T\tau_d)^2} = \frac{d\hat{\Phi}}{dN_T}.$$

SNR of a QIS

The variance of the QIS flux estimator can be computed numerically using the binomial probability mass function of N_T. For convenience, a closed form expression can be derived using a Gaussian approximation, similar to the approximation techniques used for deriving the SNR of a PF-SPAD pixel in Equation (S8). The Gaussian approximation to a binomial distribution suggests N_T has a normal distribution with mean $N\,(1 - e^{-q\Phi\tau_b})$ and variance $N\,e^{-q\Phi\tau_b}(1 - e^{-q\Phi\tau_b})$. Next, the c.d.f. of the estimated flux is given by:

$$
\begin{aligned}
F_{\hat{\Phi}_{\text{QIS}}}(x) &= \mathsf{Pr}(\hat{\Phi}_{\text{QIS}} \le x) \\
&= \mathsf{Pr}\left(-\frac{1}{q\tau_b}\log\left(1-\frac{N_T}{N}\right) \le x\right) \\
&= \mathsf{Pr}(N_T \le (1-e^{-xq\tau_b})N) \\
&= \frac{1}{2}\left(1+\operatorname{erf}\left(\frac{N(1-e^{-xq\tau_b})-N(1-e^{-\Phi q\tau_b})}{\sqrt{2}\sqrt{N(1-e^{-\Phi q\tau_b})e^{-\Phi q\tau_b}}}\right)\right) && \text{(S15)}\\
&\approx \frac{1}{2}\left(1+\operatorname{erf}\left(\sqrt{N}\frac{(x-\Phi)e^{-\Phi q\tau_b}q\tau_b}{\sqrt{2(1-e^{-\Phi q\tau_b})e^{-\Phi q\tau_b}}}\right)\right) && \text{(S16)}\\
&= \frac{1}{2}\left(1+\operatorname{erf}\left(\frac{x-\Phi}{\sqrt{2}\sqrt{\frac{(1-e^{-\Phi q\tau_b})}{q^2T\tau_b e^{-\Phi q\tau_b}}}}\right)\right) && \text{(S17)}
\end{aligned}
$$

where Equation (S15) follows from the formula for the c.d.f. of a Gaussian distribution and Equation (S16) is obtained after making a Taylor series approximation. The final form of Equation (S17) suggests that the estimated photon flux follows a normal distribution with variance $\frac{(1-e^{-\Phi q\tau_b})}{q^2T\tau_b e^{-\Phi q\tau_b}}$.

The read noise of each jot affects the RMSE of the QIS sensor at low incident flux. We note that at low flux values there are, on average, $q\Phi T$ bins already filled by true photon counts leaving $N - q\Phi T$ bins empty. Read noise will cause some of these empty bins to contain false positives and introduce additional noisy counts equal to $\frac{1}{2}(N-q\Phi T)\left(1+\operatorname{erf}\left(\frac{1}{2\sqrt{2}\sigma_r}\right)\right)$, where σ_r is the read noise standard deviation. This corresponds to a bias of $\frac{1}{2}(\frac{1}{q\tau_b}-\Phi)\left(1-\operatorname{erf}\left(\frac{1}{2\sqrt{2}\sigma_r}\right)\right)$ in the estimated photon flux. Incorporating this bias term together with the variance associated with the Gaussian distribution of the estimated photon flux, the RMSE is given by

$$
\mathsf{RMSE}(\hat{\Phi}_{\text{QIS}}) = \sqrt{\max\left\{0, \frac{1}{2}\left(\frac{1}{q\tau_b}-\Phi\right)\left(1-\operatorname{erf}\left(\frac{1}{2\sqrt{2}\sigma_r}\right)\right)\right\}^2 + \frac{1-e^{-q\Phi\tau_b}}{q^2T\tau_b e^{-q\Phi\tau_b}}}.
$$

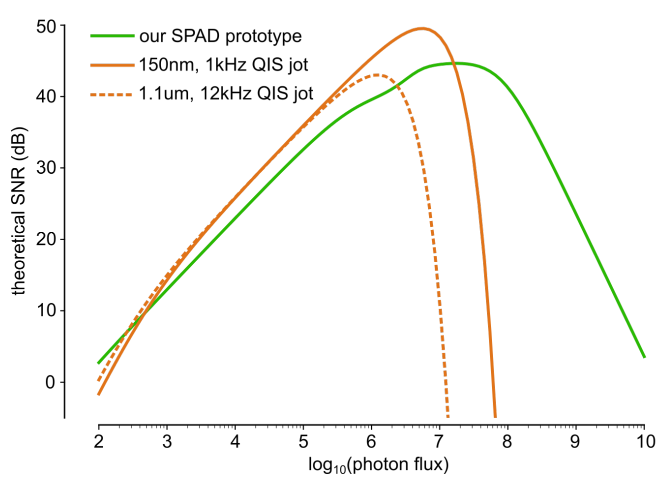

Supplementary Figure 6. **Theoretical SNR curves for a SPAD pixel compared to the effective SNR of a QIS jot block occupying the same area as the SPAD pixel.** Each QIS jot has a read noise standard deviation of 0.13 electrons and quantum efficiency of 80%. The SPAD pixel has a dead time of 150 ns, dark count rate of 100 photons/s, 40% quantum efficiency and 1% afterpulsing rate. A fixed exposure time of 5 ms is assumed for both types of pixels. Sub-diffraction limit jot sizes of under 150 nm will be required to obtain similar dynamic range as a single 25 µm SPAD pixel.

A single jot only generates a binary output and must be combined into a jot-cube to generate the final image. One way to obtain a fair comparison between a PF-SPAD pixel and a jot-cube is computing the SNR for a fixed image pixel size and fixed exposure time. We use a square grid of jots that spatially occupy the same area as our single PF-SPAD pixel that has a pitch of $25\,\mu\mathrm{m}$. Supplementary Figure 6 shows the SNR curves obtained using our theoretical derivations for a QIS jot-cube and a single PF-SPAD pixel. State of the art jot arrays are limited to a pixel size of around $1\,\mu\mathrm{m}$ and frame rates of a few kHz. These SNR curves show that we will require large spatio-temporal oversampling factors and extremely small jots to obtain similar dynamic range as a single PF-SPAD pixel. For example, a $150\,\mathrm{nm}$ jot size can accommodate almost 30,000 jots in a $25{\times}25\,\mu\mathrm{m}^2$ area occupied by the PF-SPAD pixel and can provide similar dynamic range and higher SNR than our PF-SPAD pixel when operated at a frame rate of 1 kHz. QIS technology will require an order of magnitude increase in frame readout rate or an order of magnitude reduction in jot size to bring it closer to the dynamic range achievable with our PF-SPAD prototype.

Supplementary Note 10. Additional Simulated and Experimental Results

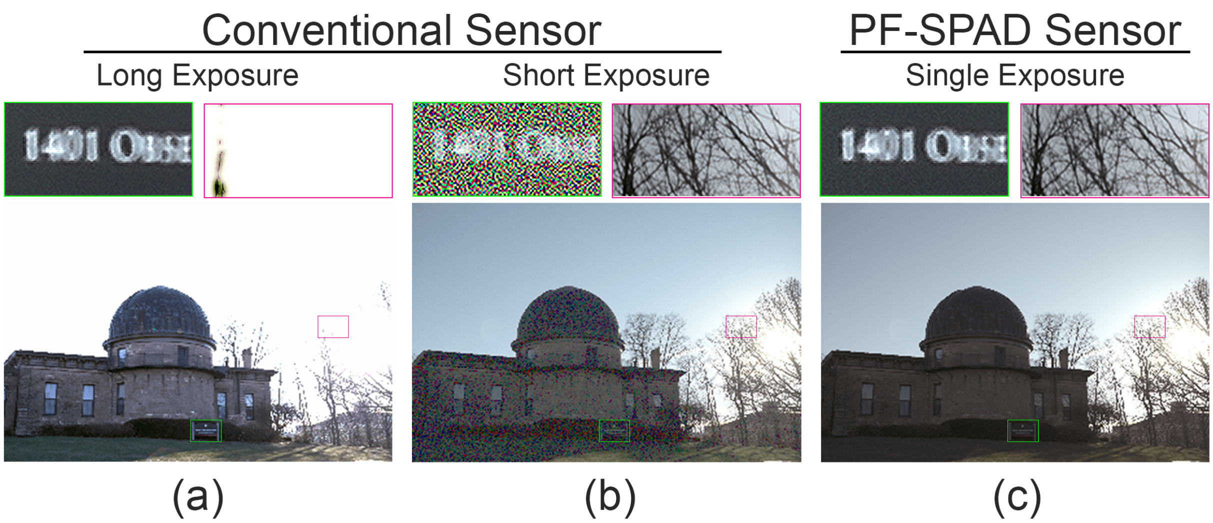

Supplementary Figure 7. **Simulation-based comparison of a conventional image sensor and a PF-SPAD on a high dynamic range scene.** The ground truth high dynamic range image was obtained using a DSLR camera with exposure bracketing over 10 stops. (a) Simulated $5\,\mathrm{ms}$ exposure image of the scene obtained using a conventional camera sensor. (b) Simulated $50\,\mu\mathrm{s}$ exposure time image using a conventional camera. (c) Simulated SPAD image of the same scene acquired with a single $5\,\mathrm{ms}$ exposure captures the full dynamic range in a single shot. Identical tone-mapping was applied to all images and zoomed insets for a fair comparison and reliable visualization of the entire dynamic range.

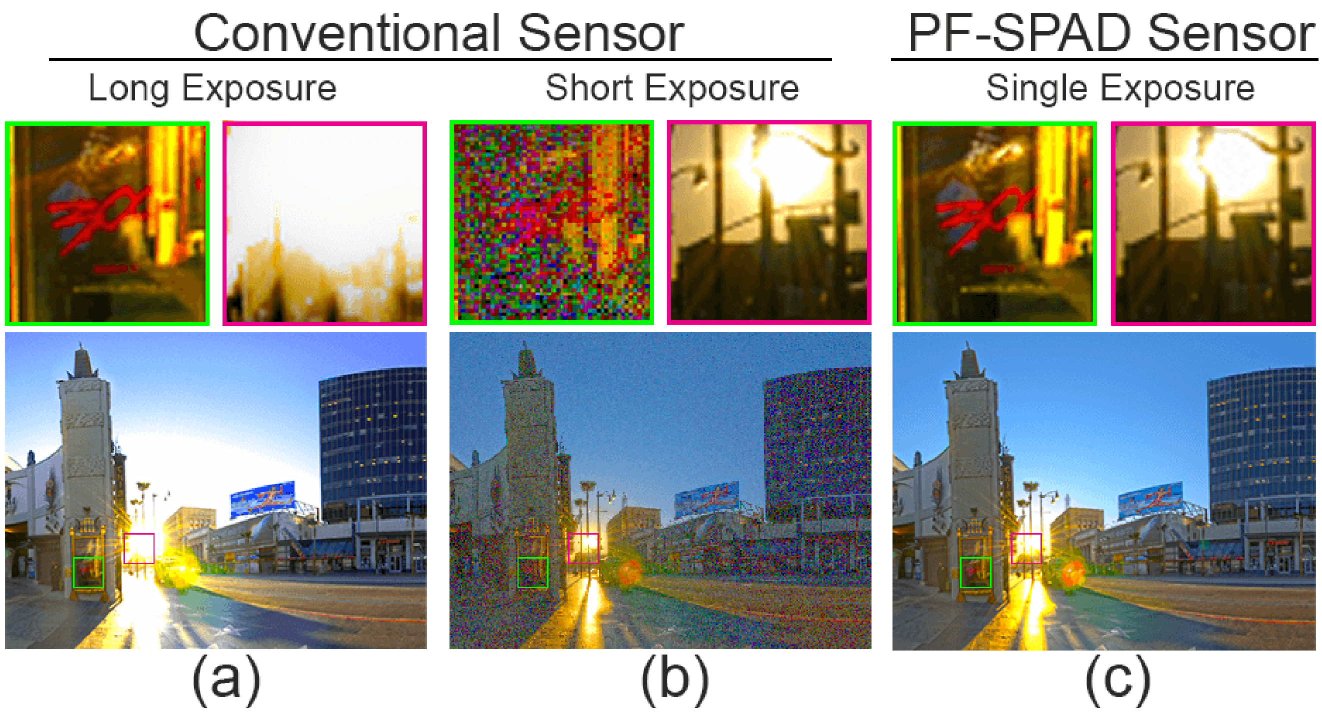

Supplementary Figure 8. **Simulated outdoor HDR scene.** (a) Long exposure capture using a conventional camera captures darker regions of the scene but the regions around the sun are saturated. (b) Short exposure time capture using a conventional sensor prevents the sun-lit region from appearing saturated but results in lost information in the shadows. (c) A single capture using a simulated PF-SPAD array circumvents the problem of low dynamic range by simultaneously capturing both highlights and shadows. Original HDR image was obtained from the sIBL datasets website `www.hdrlabs.com/sibl/archive.html`.

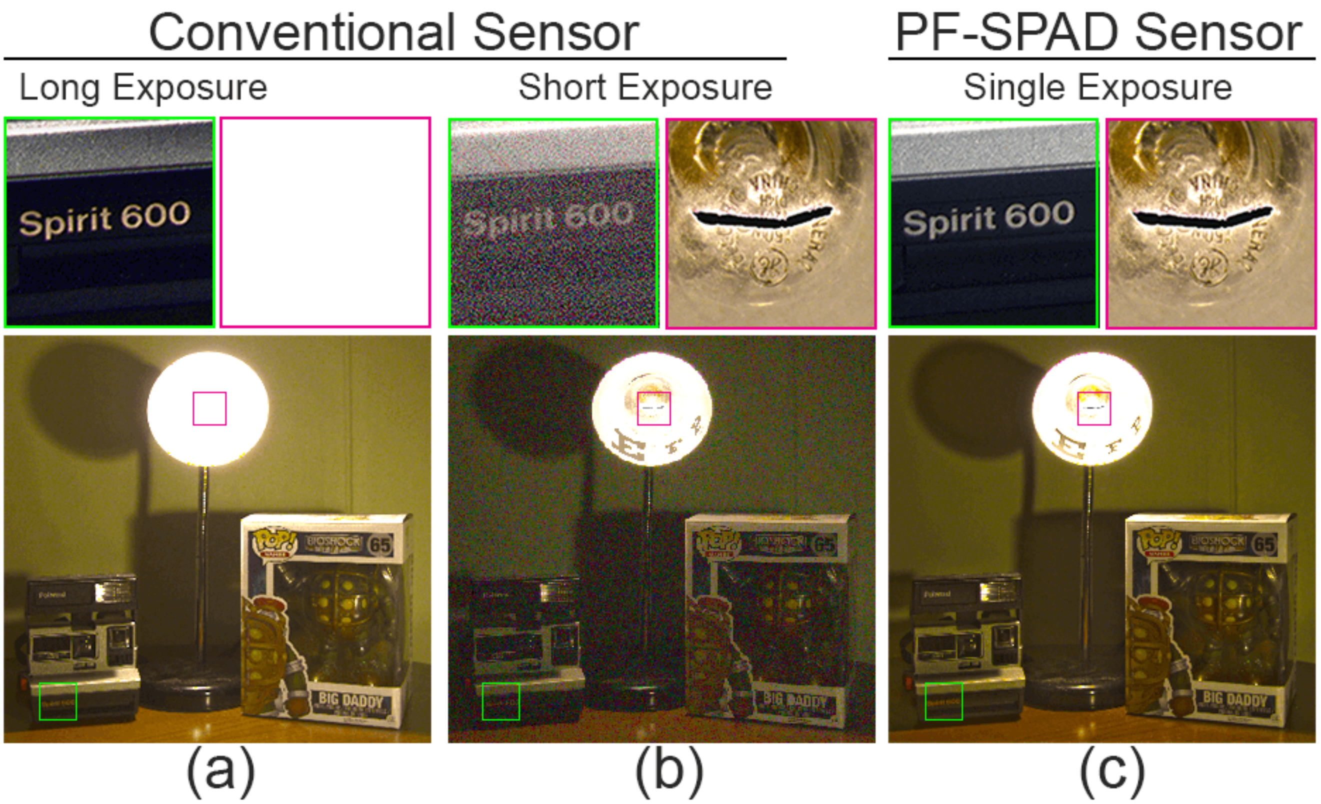

Supplementary Figure 9. **Simulated indoor HDR scene.** (a) Long exposure capture using a conventional camera captures darker regions of the scene but the regions around the bulb are completely saturated. (b) Short exposure time capture using a conventional sensor shows details of bulb filament but darker regions of the scene appear grainy due to underexposure. (c) A single capture using a PF-SPAD captures both bright and dark regions simultaneously. The original HDR image was captured using a Canon EOS Rebel T5 DSLR camera with 10 stops and rescaled to cover $10^6 : 1$ dynamic range.

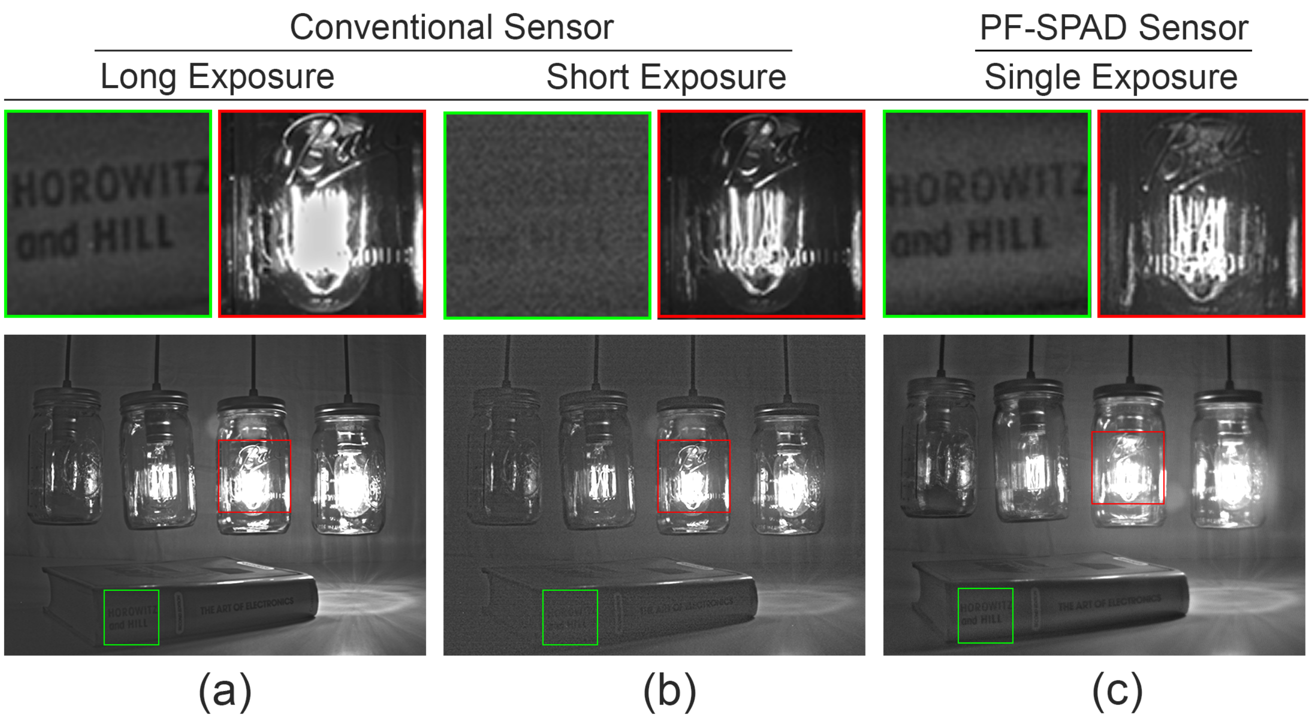

Supplementary Figure 10. **Comparison of the dynamic range of images captured using a conventional camera and our PF-SPAD hardware prototype.** (a) Long exposure ($5\,\mathrm{ms}$) shot using a conventional camera captures darker regions of the scene such as the text but the regions around the bulb filaments appear saturated. (b) Short exposure time ($0.5\,\mathrm{ms}$) capture using a shows filaments of all bulbs but leaves the darker part of the scene such as the book underexposed. (c) A single $5\,\mathrm{ms}$ exposure shot using the SPAD prototype captures the entire dynamic range. The bright bulb filament and dark text on the book are simultaneously visible.

Supplementary References

[1] Abramowitz, M. & Stegun, I. A. *Handbook of Mathematical Functions: With Formulas, Graphs, and Mathematical Tables*, vol. 55 (Dover American Nurses Association Publications, 1964), 9 edn.

[2] Antolovic, I. M., Bruschini, C. & Charbon, E. Dynamic range extension for photon counting arrays. *Optics Express* **26**, 22234–22248 (2018).

[3] Casella, G. & Berger, R. L. *Statistical Inference* (Pacific Grove, CA: Duxbury/Thomson Learning, 2002), 2nd edn. Sec. 5.5.4.

[4] Dutton, N. A. W. *et al.* A SPAD-based QVGA image sensor for single-photon counting and quanta imaging. *IEEE Transactions on Electron Devices* **63**, 189–196 (2016).

[5] Fossum, E., Ma, J., Masoodian, S., Anzagira, L. & Zizza, R. The quanta image sensor: Every photon counts. *Sensors* **16**, 1260 (2016).

[6] Grimmett, G. R. & Stirzaker, D. R. *Probability and Random Processes* (Oxford University Press, 2001), 3rd edn.

[7] Hasinoff, S. W. et al. Noise-Optimal Capture for High Dynamic Range Photography. Proc. 23rd IEEE Conference on Computer Vision and Pattern Recognition (CVPR), pp. 553–560 (2010).

[8] Itzler, M. A. Apparatus comprising a high dynamic range single-photon passive 2D imager and methods therefor (2017).